

## Article

# Assessment of Estimated Phycocyanin and Chlorophyll-a Concentration from PRISMA and OLCI in Brazilian Inland Waters: A Comparison between Semi-Analytical and Machine Learning Algorithms

Thainara Munhoz Alexandre de Lima <sup>1,2,\*</sup>, Claudia Giardino <sup>3,4</sup>, Mariano Bresciani <sup>3</sup>,  
Claudio Clemente Faria Barbosa <sup>1,2</sup>, Alice Fabbretto <sup>3,5</sup>, Andrea Pellegrino <sup>3</sup> and Felipe Nincao Begliomini <sup>6</sup>

- <sup>1</sup> Earth Observation and Geoinformatics Division (DIOTG), National Institute for Space Research (INPE), São José dos Campos 12227-010, SP, Brazil
  - <sup>2</sup> Instrumentation Laboratory for Aquatic Systems (LabISA), Earth Sciences General Coordination of the National Institute for Space Research (INPE), São José dos Campos 12227-010, SP, Brazil
  - <sup>3</sup> CNR-IREA, National Research Council of Italy, Institute for Electromagnetic Sensing of the Environment, 20133 Milan, Italy
  - <sup>4</sup> NBFC, National Biodiversity Future Center, 90133 Palermo, Italy
  - <sup>5</sup> Tartu Observatory, University of Tartu, 50411 Tartu, Estonia
  - <sup>6</sup> Cambridge Centre for Carbon Credits, Department of Computer Science and Technology, University of Cambridge, Cambridge CB2 1TN, UK
- \* Correspondence: thaimunhoz98@gmail.com

**Abstract:** The aim of this work is to test the state-of-the-art of water constituent retrieval algorithms for phycocyanin (PC) and chlorophyll-a (chl-a) concentrations in Brazilian reservoirs from hyperspectral PRISMA images and concurrent in situ data. One near-coincident Sentinel-3 OLCI dataset has also been considered for PC mapping as its high revisit time is a relevant element for mapping cyanobacterial blooms. The testing was first performed on remote sensing reflectance ( $R_{rs}$ ), as derived by applying two atmospheric correction methods (6SV, ACOLITE) to Level 1 data and as provided in the corresponding Level 2 products (PRISMA L2C and OLCI L2-WFR). Since PRISMA images were affected by sun glint, the testing of three de-glint models was also performed. The applicability of Semi-Analytical (SA) and Mixture Density Network (MDN) algorithms in enabling PC and chl-a concentration retrieval was then tested over three PRISMA scenes; in the case of PC concentration estimation, a Random Forest (RF) algorithm was further applied. Regarding OLCI, the SA algorithm was tested for PC estimation; notably, only SA was calibrated with site-specific data from the reservoir. The algorithms were applied to the  $R_{rs}$  spectra provided by PRISMA L2C products—and those derived with ACOLITE, in the case of OLCI—as these data showed better agreement with in situ measurements. The SA model provided low median absolute error (Mdae) for PRISMA-derived (Mdae = 3.06 mg.m<sup>-3</sup>) and OLCI-derived (Mdae = 3.93 mg.m<sup>-3</sup>) PC concentrations, while it overestimated PRISMA-derived chl-a (Mdae = 42.11 mg.m<sup>-3</sup>). The RF model for PC applied to PRISMA performed slightly worse than SA (Mdae = 5.21 mg.m<sup>-3</sup>). The MDN showed a rather different performance, with higher errors for PC (Mdae = 40.94 mg.m<sup>-3</sup>) and lower error for chl-a (Mdae = 23.21 mg.m<sup>-3</sup>). The results overall suggest that the model calibrated with site-specific measurements performed better and indicates that SA could be applied to PRISMA and OLCI for remote sensing of PC in Brazilian reservoirs.

**Keywords:** cyanobacteria; phycocyanin; machine learning; semi-analytical model; aquatic remote sensing; hyperspectral



**Citation:** Lima, T.M.A.d.; Giardino, C.; Bresciani, M.; Barbosa, C.C.F.; Fabbretto, A.; Pellegrino, A.; Begliomini, F.N. Assessment of Estimated Phycocyanin and Chlorophyll-a Concentration from PRISMA and OLCI in Brazilian Inland Waters: A Comparison between Semi-Analytical and Machine Learning Algorithms. *Remote Sens.* **2023**, *15*, 1299. <https://doi.org/10.3390/rs15051299>

Academic Editor: Cédric Jamet

Received: 15 January 2023

Revised: 20 February 2023

Accepted: 24 February 2023

Published: 26 February 2023



**Copyright:** © 2023 by the authors. Licensee MDPI, Basel, Switzerland. This article is an open access article distributed under the terms and conditions of the Creative Commons Attribution (CC BY) license (<https://creativecommons.org/licenses/by/4.0/>).

## 1. Introduction

Access to clean water is one of the 17 Sustainable Development Goals of the Agenda 2030 elaborated and agreed upon by the member countries of the United Nations, to which

Brazil is a signatory [1]. Despite the crucial importance of preserving continental aquatic systems, intense human activities have promoted the eutrophication of water bodies, leading to a significant increase in phytoplankton biomass and the frequency of algal blooms, including potentially harmful cyanobacterial algae (CyHAB) [2]. In particular, regular and continuous CyHAB monitoring is necessary to assess and mitigate environmental changes, as well as to support informed decisions and evidence-based policies for the efficient use of the planet's resources [3,4]. In this context, the use of remote sensing techniques provides advantages for observing spatio-temporal dynamics, with a synoptic and high-temporal-resolution view of a feature of interest, yielding the basis for reliable and accountable scientific understanding and knowledge of phytoplankton dynamics [5–7]. Multispectral sensors such as Sentinel-2 Multispectral Instrument (MSI) and Sentinel-3 Ocean and Land Color Instrument (OLCI) have been largely used for mapping the concentration of the primary absorption pigment of phytoplankton, chlorophyll-a (chl-a), in lakes and freshwater reservoirs [8–10]. Moreover, hyperspectral remote sensing is contributing to phytoplankton pigment mapping with dedicated algorithms [11] making use of continuous and dense spectral sampling. The benefits of merging hyperspectral imagery with the consolidated multispectral data will support future efforts to deal with, for example, the response of freshwater ecosystems to population growth and climate change [12].

Assertive indicators for the presence of CyHABs using satellite data have been chl-a and phycocyanin (PC), an auxiliary photosynthetic pigment with major presence in cyanobacteria [9,13]. Due to PC's specific absorption features, and by considering the challenging nature of retrieving water constituents in inland waters [14–16], remote sensing of freshwater cyanobacteria biomass has been largely focused on algorithms developed on hyperspectral reflectance [17–21]. In particular, for the retrieval of PC, Simis et al. [22] presented a nested band PC hyperspectral algorithm addressing the spectral influence of chl-a in the PC absorption peak (620 nm), showing high performance in cyanobacteria-dominated temperate eutrophic waters [23–25]. More recently, machine learning (ML) algorithms have exploited the estimation of PC from spaceborne imaging spectroscopy [26] over a variety of inland water bodies.

However, when applied to satellite imagery data, the accuracy of water quality parameter retrieval depends on the successful removal of the atmospheric contributions to the signal measured by the satellite sensor. The hyperspectral retrieved remote sensing reflectance ( $R_{rs}$ ) is strongly affected by several degrees of uncertainties related to a suboptimal signal-to-noise ratio (SNR), the possible presence of sun glint, and adjacency effects [27]. These influences require the investigation and development of suitable correction models to minimize uncertainty propagation in parameter estimates.

In this scenario, the use of PRISMA (PRecurso IperSpettrale della Missione Applicativa), a hyperspectral satellite mission of the Italian Space Agency (ASI), has been gaining attention for water quality mapping over the last years. Niroumand-Jadidi, et al. [28], O'shea et al. [26], Bresciani et al. [29], and Borfecchia et al. [30] demonstrated the use of PRISMA for retrieving water quality parameters and bottom properties of inland waters starting from  $R_{rs}$  data. Although the radiometric resolution is suboptimal [31], the results highlighted the potential of the fine and continuous spectral information offered by PRISMA. Further applications, e.g., the retrieval of advanced products such as particle size and phytoplankton functional types, still needs to be demonstrated.

In this work, we evaluated the applicability and the accuracy of PRISMA hyperspectral imagery for mapping chl-a and PC in Brazilian inland waters with concurrent in situ measurements, testing a set of algorithms for atmospheric and sun glint corrections and for chl-a and PC concentration retrieval. Sentinel-3 OLCI, which uniquely provides daily observations, was also included for mapping PC. In particular we assessed the performance of the atmospheric correction (AC) models ACOLITE [32] and 6SV [33], along with  $R_{rs}$  measurements from PRISMA Level 2 and OLCI standard products. Since one PRISMA image was affected by sun glint, three well-established methods were applied to remove it. Subsequently, a semi-analytical model and two ML approaches to estimate chl-a and PC

concentrations were tested and validated with in situ measurements. This work is expected to extend PRISMA product exploitation for mapping chl-a and PC in tropical freshwater reservoirs, allowing for the improvement in the application of EO data for water quality monitoring and management.

## 2. Study Area

Brazil is among the nine richest countries in freshwater reserves, representing almost 12% of the total volume of freshwater available. Despite the great water availability, the distribution of this resource is not performed in an equitable way, since 70% of water production is concentrated in the Amazon Basin. Much of this reserved water in Brazil is intended for the production of electricity, as the country's energy is highly dependent on hydroelectricity [34]. The main Brazilian hydroelectric reservoirs are in the Paraná River Basin (57 reservoirs), which represents 6% of Brazilian water production. One of the main tributaries of the Paraná Basin is the Tietê River, which crosses the state of São Paulo (Figure 1a). Considering its 1100 km of extension, the Tietê Cascade System Reservoir (TCSR) includes six reservoirs, accumulating 29,100 m<sup>3</sup> of water. The TCSR's waters are deeply affected by different non-natural contamination sources, such as discharge from pasture waste, wastewater from urban centers, and other agricultural activities developed in nearby areas, including sugarcane and citrus crops [35].

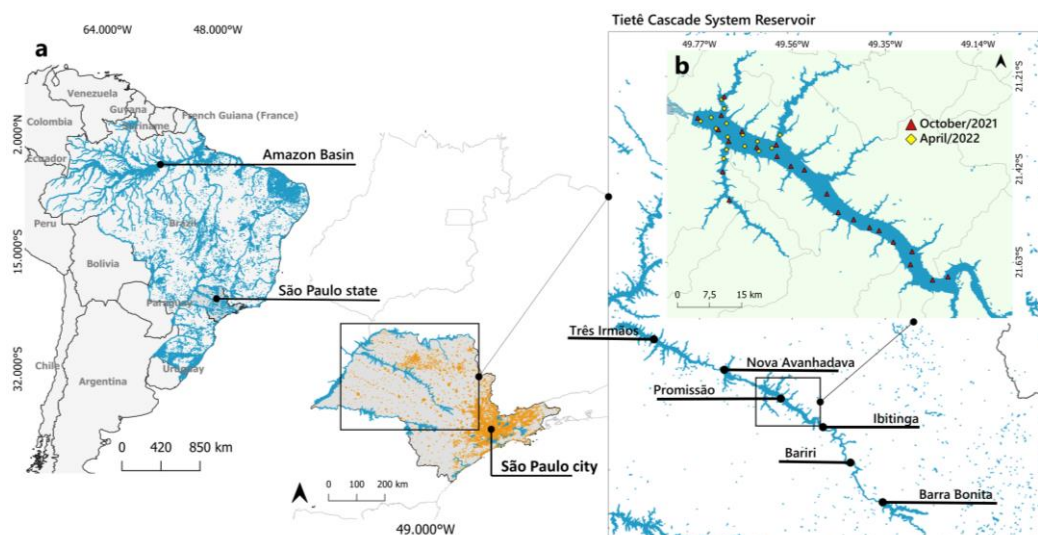


**Figure 1.** (a) Brazilian rivers; highlight for the state of São Paulo and the Tietê Cascade System. (b) Promissão Reservoir. Red and yellow points highlighted in Promissão Reservoir correspond to samples measured during the field campaigns in October/2021 and April/2022.

This study focuses on Promissão Reservoir (Figure 1b), which is the fourth largest reservoir in the TCSR. It has 560 km<sup>2</sup> of flooded area, 57,610 km<sup>2</sup> of drainage, and 134.1 days, on average, of residence time.

## 3. Dataset

### 3.1. Field Measurements

The field data considered in this study were gathered during two campaigns performed in October 2021 and April 2022, covering 23 and 15 stations, respectively (Figure 1b), and include both radiometric and phytoplankton data.

A set of three Trios-Ramses spectroradiometers, ranging from 400–900 nm with a sampling interval of 3.3 nm and positioned on top of the boat, was used to collect radiometric data across the Promissão Reservoir: two Ramses-ARC radiance radiometers sensors with 7° Field-of-View (FOV), and one Ramses-ACC irradiance radiometer equipped with a cosine collector pointed up. The instruments measured the downward irradiance ( $E_s$ );

the 25 angles of each sensor were pre-established following the protocol proposed by Mobley [36] to minimize the specular reflection effects of direct and diffuse radiation. These quantities allowed us to compute the  $R_{rs}$  according to the SeaWiFS protocol [37], wherein residual glint effects of the  $R_{rs}$  spectrum were corrected according to Kutser et al. [38] and Cairo et al. [16]. After glint correction, each  $R_{rs}$  spectrum was spectrally resampled according to both OLCI and PRISMA spectral response functions (SRFs) [39].

### Laboratory Analysis

Water samples for phytoplankton analyses were collected at the topmost layers of the water and placed in dark bottles until lab analysis. The water samples were filtered onto GF/F filters (Whatman, 47 mm diameter, 0.7  $\mu\text{m}$  pore) under low-light conditions and low vacuum. The samples were filtered in duplicates of 100–500 mL of water. Then, the filters were placed into a 15 mL Falcon tube and frozen at  $-80\text{ }^{\circ}\text{C}$  until analysis. The spectral absorption due to phytoplankton ( $a_{phy}$ ) was measured according to Tassan and Ferrari [40], Roesler [41], and Stramski [42].

The Chl-a concentration was derived according to the American Public Health Association, APHA [43]. After filtration, the GF/F filters were homogenized and the pigments extracted using 90% acetone. The phytoplankton pigment concentration was calculated by Lorenzen's equation [43]. PC was quantified in the water samples by following the method described by Sarada et al. [44] and adapted by Horváth et al. [45]. Before carrying out the analysis, the filters were suspended in a phosphate buffer (100 mM and pH 7.2) and submitted to three freeze–thaw cycles ( $-80\text{ }^{\circ}\text{C}$  and  $35\text{ }^{\circ}\text{C}$ ). The samples were then sonicated (90 s at a frequency of 20 kHz) and centrifuged (30 min at 3000 rpm). PC concentration was calculated using the equation found in [46], considering the obtained spectrophotometric measurements (Table 1).

**Table 1.** Descriptive statistics from phycocyanin ( $\text{mg}\cdot\text{m}^{-3}$ ) and chlorophyll-a ( $\text{mg}\cdot\text{m}^{-3}$ ).

		Min	Max	Mean	Median	Std
October/ 2021	PC	0.33	136.39	10.01	3.00	27.20
	Chl-a	25.44	183.47	66.51	50.04	41.00
	PC:Chl-a	0.008	0.74	0.095	0.073	0.14
April/ 2022	PC	1.36	65.89	26.98	18.16	19.23
	Chl-a	15.59	487.82	167.45	115.76	138.57
	PC:Chl-a	0.074	0.47	0.18	0.15	0.10

## 3.2. Satellite Imagery Data

### 3.2.1. PRISMA

PRISMA is a satellite mission funded by ASI and in orbit since in March 2019. The satellite payload is composed of an imaging spectrometer able to capture images at 30 m spatial resolution in a spectral continuum of 239 spectral bands between 400–2500 nm (66 in the Visible and Near-Infrared (VNIR) and 173 in the Short Wave Infra-Red (SWIR) spectrum) [47]. The imagery products are released with different levels of pre-processing. Notably, the Level 1 (L1) products are radiance imagery at the Top-of-Atmosphere (TOA) organized in two radiometrically and geometrically calibrated hyperspectral and panchromatic radiances cubes; then, a series of Level 2 (L2) products are also available as atmospherically corrected hypercube and panchromatic Bottom-of-Atmosphere (BOA) reflectance. PRISMA L1 products were used as input in the AC methods, while L2C products were already offering atmospherically corrected reflectance for evaluation.

### 3.2.2. OLCI

Launched in 2016 (Sentinel-3A) and 2018 (Sentinel-3B), OLCI is a multispectral radiometer, with 21 bands (400–1020 nm), high SNR (between 305 and 2188), and an approx-

imately 300 m spatial resolution. In this study, we use L1B Full-Resolution Product as input to the AC models, and L2 Water Full-Resolution Product (Water Surface Reflectance). Level-1B Product provides calibrated, ortho-geolocated and spatially re-gridded TOA radiances, while Level-2 Water Product provides water-leaving radiance as well as water and atmospheric geophysical products [48].

### 3.2.3. Available Dataset

Three PRISMA and OLCI cloud-free scenes of the Promissão Reservoir acquired on 3 October 2021, 4 September 2021, and 26 July 2022 were considered in this study. The images acquired on 3rd, October, 2021 were co-located with four field stations visited within  $\pm 1$  day of PRISMA and OLCI overpass with no significant changes in the water color, and were used to validate the atmospheric and glint correction models and the PC algorithms. The images acquired on 4 September 2021 and 26 July 2022 were used to further apply the calibrated models to compare the PC estimates between hyperspectral and multispectral sensors.

## 4. Methods

### 4.1. Satellite Imagery Processing

#### 4.1.1. Atmospheric Correction

Here, a comparison of the satellite-retrieved surface reflectance with in situ data was performed to better understand how uncertainties in AC propagate in multispectral and hyperspectral satellite data. Following this, the four AC methods presented here were tested: PRISMA L2C processor, OLCI L2-WFR, 6SV, and ACOLITE. Among the models tested, PRISMA L2C and OLCI L2-WFR correspond to standard Level-2 products of PRISMA and OLCI, respectively, while 6SV and ACOLITE were applied to the TOA images (Level-1). For all AC models tested, the corrected surface reflectance image was divided by  $\pi$  (3.1415) in order to obtain the atmospherically corrected  $R_{rs}$ .

- Standard PRISMA L2C processor: The L2 standard AC processor is based on MODTRAN v6.0, using a multi-dimensional Look-Up-Table (LUT) approach [27]. This method uses the hyperspectral bands to derive atmospheric parameters (e.g., water vapor and Aerosol Optical Depth (AOD)). The water vapor is retrieved pixel-by-pixel using the water's absorption features at NIR bands. The retrieval of PRISMA AOD is based on the Dense Dark Vegetation (DDV) algorithm approach [49], exploiting the correlation between reflectance in the SWIR region, blue, and red bands. An extended description of the algorithms used to generate PRISMA products is available in [50].
- OLCI L2-WFR: The baseline AC algorithm (BAC) used in OLCI L2 products is a combination of NIR-based black-pixel assumption with bright-pixel AC (BPAC). BPAC corrects the contribution of sediments when the water-leaving reflectance is no longer negligible in NIR bands, as is the case for coastal and inland turbid waters. It consists of decoupling the oceanic and atmospheric components of the NIR bands in order to apply the standard AC scheme [51].
- 6SV (for both PRISMA and OLCI): Second Simulation of a Satellite Signal in the Solar Spectrum (6SV) is an advanced radiative transfer code designed to simulate a specific condition of the atmosphere based on advance knowledge of atmospheric and illumination conditions and the sensor used. The algorithm takes as input the necessary parameters to apply the radiative transfer equation for estimating the surface reflectance [32]. For the validation of PRISMA L1 and OLCI L1 products, 6SV was applied using the Py6S Python programming language interface [52]. The aerosol and atmospheric profiles were set as Continental and Tropical, respectively. The AOD (550) value and the geometry parameters were obtained from PRISMA metadata. The correction was made for each PRISMA and OLCI band using their respective SRFs.
- ACOLITE (for both PRISMA and OLCI): The current version of ACOLITE (20220222.0) applies a dark spectrum fitting (DSF) scheme as the default setting to estimate the AOD and, hence, atmospheric path reflectance, transmittances, and spherical albedo [33].

The DSF assumes: (i) a homogeneous atmosphere over a certain extent of an image, and (ii) that there are pixels within this subscene that contain near-zero water-leaving radiances in one band. A pre-generated LUT is utilized to find the dominant aerosol condition. Despite being primarily designed for processing multispectral images, ACOLITE is now adapted to support processing of PRISMA data where the L1 and L2C data products are required as inputs. The ACOLITE/DSF processing (version 20220222.0) is available in a GitHub code repository and in binary releases (<https://github.com/acolite/acolite>, accessed on 25 February 2023).

#### 4.1.2. Glint Correction

In order to evaluate the influence of glint on the reflectance spectrum, three different glint correction methods were applied in all PRISMA atmospherically corrected products to choose the best possible combination for the assessed sensors:

- The Wang and Shi [53] (WS07) method assume that the reflectance values of SWIR bands come from the specular reflection in the water's surface (sun and sky glint), as the signal from this spectral region is considered negligible in natural inland waters [26]. Considering the 173 SWIR channels from PRISMA (942–2496 nm), a SWIR-range band centered near 1600 nm [1533.56–1745.93 nm] was considered as the reference band for performing the glint correction. In principle, a band range centered near 2200 nm could also be selected as reference. However, these bands are much noisier than 1600 nm [54]. Therefore, in order to avoid the possible noise propagation to the glint-removed bands in the visible region, the 1600 nm SWIR band was selected as the reference band, where the average was considered and then subtracted from each band in the VNIR spectrum.
- The Hedley et al. [55] (HED05) method assumes negligible water-leaving signal in the NIR part of the spectrum. Relative sun-glint intensity of the image is obtained based on the NIR brightness and the light in the visible band using a set of pixels, which could be homogeneous if not for the presence of glint. Establishing a linear relationship between the NIR band and each visible band allows for the removal of the glint contribution. In case of hyperspectral data there is a need to find the regression algorithm for each spectral band. The HED05 method was used in a deglint processor implemented in the Sen2Coral toolbox available in the SNAP software (<https://sen2coral.argans.co.uk/>, accessed on 25 February 2023). Bands between 833–972 nm were considered as glint reference.
- Kutser et al. [56] (KUT09) proposed an alternative glint removal procedure for hyperspectral imagery when SWIR data is not available. The method is based on the assumption that there is no spectral feature in the  $R_{rs}$  at 760 nm if it does not contain glint. Furthermore, it considers that the depth of an oxygen absorption feature at 760 nm (called D) is proportional to the amount of glint in this pixel. The model assumes that pixels with D values close to zero do not contain glint and pixels with the highest D value contain mainly glint. By subtracting the pixel spectrum in which D is close to zero from the spectrum with the highest D, the glint spectrum is obtained. In order to avoid land pixels or adjacency pixels, before the application of the model, a water mask must be applied.

#### 4.1.3. Performance Assessment (Radiometry)

Considering the match-up samples ( $N = 4$ ) between the satellite overpass (PRISMA and Sentinel-3A/B) and in situ measurements on 3rd, October, 2021, atmospheric and glint correction models were assessed qualitatively by comparing in situ  $R_{rs}$  measurements (resampled to PRISMA and OLCI bands) against satellite-derived surface  $R_{rs}$  and quantitatively through the coefficient of determination ( $R^2$ ), Bias, Root Mean Square Error (RMSE), Mean Absolute Percentage Error (MAPE), and the Spectral Angle (SA) (Table 2). SA was used to determine the spectral similarity between satellite-derived surface  $R_{rs}$  and in situ

$R_{rs}$  (lower SA indicates higher similarity), since SA is not sensitive to differences in the magnitude of spectrums.

**Table 2.** Formulas for error metrics, where  $y_i$  and  $x_i$  represent atmospherically and glint-corrected  $R_{rs}$  and in situ  $R_{rs}$ , respectively.

<b>Coefficient of Determination</b>	$R^2 = \left[ \frac{\sum_{i=1}^n (x_i - \bar{x})(y_i - \bar{y})}{\sqrt{\sum_{i=1}^n (x_i - \bar{x})^2} \sqrt{\sum_{i=1}^n (y_i - \bar{y})^2}} \right]^2$
<b>Bias</b>	$Bias = \frac{\sum_{i=1}^n \left( \frac{y_i - x_i}{x_i} \right)}{n} \times 100$
<b>Root Mean Square Error (RMSE)</b>	$RMSE = \sqrt{\frac{\sum_{i=1}^n (y_i - x_i)^2}{n}}$
<b>Mean Absolute Percentage Error (MAPE)</b>	$MAPE = \frac{100}{n} \sum_{i=1}^n \left  \frac{y_i - x_i}{x_i} \right $
<b>Spectral Angle (SA)</b>	$SA = \cos^{-1} \frac{\sum_{i=1}^n y_i x_i}{\sqrt{\sum_{i=1}^n y_i^2} \sqrt{\sum_{i=1}^n x_i^2}}$

#### 4.2. Phycocyanin and Chlorophyll-a Modeling

Two approaches were used to retrieve PC and Chl-a concentrations from radiometric data: semi-analytical algorithms and ML models. They are outlined below.

##### 4.2.1. Nested Band Semi-Analytical Algorithm

The most widely used semi-analytical algorithm to estimate PC concentration was developed by Simis et al. [22] (SIMIS05). The SIMIS05 algorithm assumes that the absorption at 620 nm is determined mainly by PC concentration with some spectral contribution from Chl-a (absorption peak at 665 nm). The algorithm attempts to isolate PC absorption by relating the reflectance at 620 nm with wavelengths without pigment absorption features (e.g., 709 nm and 779 nm) and removing the Chl-a spectral influence by empirically estimating the absorption of Chl-a at 620 nm from the 665 nm coefficient [22]:

$$a_{pc}(620) = \left[ \frac{R_{rs}(709)}{R_{rs}(620)} * (a_w(709) + b_b) - b_b - a_w(620) \right] * \delta^{-1} - (\varepsilon * a_{chla}(665)), \quad (1)$$

where  $a_w$  is the absorption by water ( $a_w(620) = 0.281 m^{-1}$ );  $\delta$  is a correction factor to relate the  $R_{rs}$  ratio to measured pigment absorption; and  $\varepsilon$  is a conversion factor that relates the absorption of Chl-a at 665 nm with its absorption at 620 nm. The backscattering ( $b_b$ ) is assumed to be spectrally neutral and was derived by Simis et al. [22] from  $R_{rs}$  at a single wavelength in the near infra-red [57]. Here, we apply  $b_b(700) = 0.1345$  estimated by in situ measurements using the multispectral sensor HydroScat-6, by Hobilabs. The HydroScat-6 measures the scattering at a specific angle (140°) on six different channels, each sensitive to a narrow range of optical wavelengths (420, 442, 470, 488, 510, 550, 590, 620, 676, 700, and 852 nm). Each channel consists of a source and separate optical receptors. The source is responsible for emitting a beam of light into the water and the receptor is responsible for collecting the backscattered portion, which is then used to model the volumetric scattering function for estimating the backscattering coefficient ( $b_b$ ). The Chl-a absorption at 665 nm was calculated applying the equation developed by Gons [58] (GON99):

$$a_{chla}(665) = \left[ \frac{R_{rs}(709)}{R_{rs}(665)} * (a_w(709) + b_b) - b_b - a_w(665) \right] * \gamma^{-1} \quad (2)$$

A correction factor ( $\gamma$ ) was also introduced by Simis et al. [50] to relate the  $R_{rs}$  ratio to the measured Chl-a absorption. Finally, the PC and Chl-a concentration were calculated by dividing the absorption coefficient ( $a_{pc}(620)$ ;  $a_{chla}(665)$ ) by the specific absorption coefficient ( $a_{pc}^*(620)$ ;  $a_{chla}^*(665)$ ):

$$[PC] = \frac{a_{pc}(620)}{a_{pc}^*(620)} \quad (3)$$

$$[Chla] = \frac{a_{chla}(665)}{a_{chla}^*(665)} \quad (4)$$

In order to achieve better model performance, we reparametrized the SIMIS05 algorithm using in situ data. First, the correction factors  $\delta$  (Equation (1)) and  $\gamma$  (Equation (2)) were retrieved from in situ  $R_{rs}(\lambda)$  and  $a_{phy}(\lambda)$  spectra considering the entire dataset ( $N = 38$  samples). In this way, Equations (1) and (2) were initially applied considering  $\delta = \gamma = 1$ , obtaining an ‘uncorrected’  $a_{chla}(665)$  and  $a_{pc}(620)$ . The linear least-squares fit of the uncalibrated equations’ derived absorptions against  $a_{phy}(\lambda)$  measurements (for  $\lambda = 665$  and  $620$  nm) yielded the slopes that were adopted as the new parameters ( $\gamma = 0.14585$  and  $\delta = 0.18055$ ). The conversion factor  $\varepsilon$  (Equation (1)) was originally estimated in Simis et al. [50] from the best fit of computed versus observed PC concentration. Our in situ data were not used for calculating  $\varepsilon$  to avoid overfitting. Instead, O’Shea et al. [26] applied a dataset of 939 samples to optimize the  $\varepsilon$  value by minimizing the median symmetric accuracy between the model estimates and the known in situ concentration. The final value obtained ( $\varepsilon = 0.251753$ ) was then applied here. Finally, the specific absorption coefficient for PC at 620 nm ( $a_{pc}^*(620)$ ) and Chl-a at 665 nm ( $a_{chla}^*(665)$ ) was determined from the absorption  $a_{pc}(620)$  and  $a_{chla}(665)$  measured in-laboratory and divided by the measured PC and Chl-a concentration, respectively, for all the dataset.

#### 4.2.2. Machine Learning Models

Two ML models were used here to estimate PC concentration: (i) the MDN algorithm [26] and the Random Forest (RF) algorithm [59]. No further training based on our dataset was applied in order to estimate how well the models are expected to be transferred to regions not included within the training set.

O’Shea et al. [26] calibrated an MDN algorithm for predicting PC based on in situ radiometric measurements resampled for HICO and PRISMA sensors. The dataset consisted of 939 samples composed of in situ  $R_{rs}$ , Chl-a, and PC measurements for water bodies worldwide. In order to reduce the influence of  $R_{rs}$  uncertainties, the MDN architecture replaces the pure  $R_{rs}$  commonly used for inverse aquatic remote sensing tasks, and uses as input feature band ratios (BRs), line heights (LHs), and multispectral algorithms (MAs) (500–550, 620, 650, and 710 nm) based on their correlation with PC (Table 3). The results obtained demonstrate the robustness of the model for estimating low PC concentrations ( $<10$  mg m<sup>-3</sup>) and the reduced impact of the uncertainties derived from orbital measurements of the  $R_{rs}$  on medium-to-high in situ PC measurements ( $>10$  mg m<sup>-3</sup>). Considering the uniform accuracy for different concentration ranges and the broad number of water bodies used in the model calibration/validation, MDN is the closest from a global PC algorithm. The entire in situ  $R_{rs}$  (resampled to PRISMA bands) data and PRISMA images were used to predict PC and Chl-a using the MDN model. As the algorithm does not allow any extra training or parameter-setting, MDN was applied in default mode as provided by the authors (<https://github.com/STREAM-RS/STREAM-RS>, accessed on 25 February 2023). The model took 26 PRISMA bands (500–719 nm) as input and calculated PC and Chl-a concentration as final output.

**Table 3.** Input features used in the ML model to estimate PC concentration [26,59].

ML Model	Selected Features
MDN	MA [17] * (600, 648, 624); BR(650, 625); BR(709, 665); BR(709, 620); BR(700, 600); MA [60] * (725, 615, 600); LH(665, 681, 709); MA [61] * (724, 629, 659); LH(654, 714, 754); LH(665, 709, 754); LH(680, 709, 754); MA [62] * (709, 665); LH(560, 620, 665); LH(665, 673, 681); LH(690, 709, 720); LH(620, 650, 670); LH(640, 650, 660); LH(613, 620, 627).
RF	LH(739, 802, 855); NI(563, 555); LH(651, 699, 750); MA [61] * (531, 571, 614)

\* Multispectral algorithm to estimate PC concentration.

Begliomini [59] used radiometric in situ  $R_{rs}$  resampled to PRISMA bands, as well as biological data (PC and Chl-a) measured in eight field campaigns in the Billings Reservoirs, Brazil (115 samples), to calibrate/validate three different ML algorithms (RF, Extreme Gradient Boosting, and Support Vector Machine) using the Python language. Following the MDN model, the pure spectral bands were not used as input features to avoid atmospheric-derived uncertainties. The input features in the model calibration consisted of normalized indices (NIs), LHs, and MAs. A data-driven feature selection was first applied using the Predictive Power Score to retain only the relevant features for predicting PC. Then, the Pearson coefficient was calculated for each pair of the filtered features, and a threshold of 0.8 was established to remove the most correlated layers. Table 3 shows the selected features used in the final training model. The Monte Carlo simulation was then performed (1000 rounds), using 80% of the dataset for training and 20% for testing. The accuracy metrics were calculated for each round, and the median value for all rounds was used to assess the results. Among the ML models tested by the author, RF achieved the best performance for orbital PC retrieval (Bias = 45%). Therefore, it was chosen to be evaluated in this study for the Promissão Reservoir. Moreover, like Promissão Reservoir, Billings Reservoir is also part of the TCSRs, which allows for a better proximity for the optical behavior of the dataset used in model training. Following the application of MDN, the RF model also does not allow extra training. Thus, the entire dataset (in situ  $R_{rs}$  resampled to PRISMA bands and PRISMA image) was applied in order to validate the PC estimates.

#### 4.2.3. Performance Indicators (Algorithms)

The performances of each algorithm were assessed using in situ  $R_{rs}$  resampled to PRISMA and OLCI bands, comparing them with satellite image  $R_{rs}$  within 1 day of in situ PC and Chl-a measurements. The robustness of the relationship between the algorithm estimated values and measured values was evaluated applying linear least squares regression analysis. The goodness of fit is reported by  $R^2$  and the slope ( $p$ ). Algorithm accuracy was quantified with measures of errors, including the median symmetric accuracy ( $\zeta$ ) (Table 4), which is equivalent to the median unsigned percentage error, and the median absolute error (MdAE) (Table 4). The first norm ( $\zeta$ ) initially transform data into log space and then convert them back to linear space to assess the quality of the retrieved quantity. This transformation ensures that the metric is symmetric, i.e., a switch in the values of the predicted and observed value will result in the same error (unlike MAPE). The interpretation of the median symmetric accuracy is that 50% of the unsigned percentage errors are smaller than  $\zeta$  [63].

**Table 4.** Statistical error metrics, where  $y_i$  and  $x_i$  represent the modeled value and in situ measured value, respectively.

<b>Median Symmetric Accuracy</b>	$\zeta = 100 \times \left( \exp \left( \frac{\sum_{i=1}^n \left  \log_e \frac{y_i}{x_i} \right }{n} \right) - 1 \right)$
<b>Median Absolute Error</b>	$MdAE = \text{median}( y_i - x_i , \dots,  y_i - x_i )$

## 5. Results and Discussion

### 5.1. Atmospheric and Glint Correction

Qualitative comparisons between TOA  $R_{rs}$ , AC-derived  $R_{rs}$ , and in situ  $R_{rs}$  for PRISMA and OLCI images are presented in Figure 2 with the aim of pointing out artifacts that may characterize either satellite or in situ data. The lower bound (500 nm) was chosen to avoid commonly high uncertainties in  $R_{rs}$  within the blue region [27]. Due to the presence of high glint effect for the considered date (3 October 2021), an offset difference was highlighted in all AC models, mainly in the PRISMA image (Figure 2). Despite the offset, for both satellite imagery sets the AC processors were capable of removing most of the atmospheric effects. Before AC, the TOA  $R_{rs}$  spectrum presents an exponential behavior

indicating dominance by Rayleigh and aerosol scattering effects. After the correction, the  $R_{rs}$  spectrum shows a shape close to that of the in situ measurements.

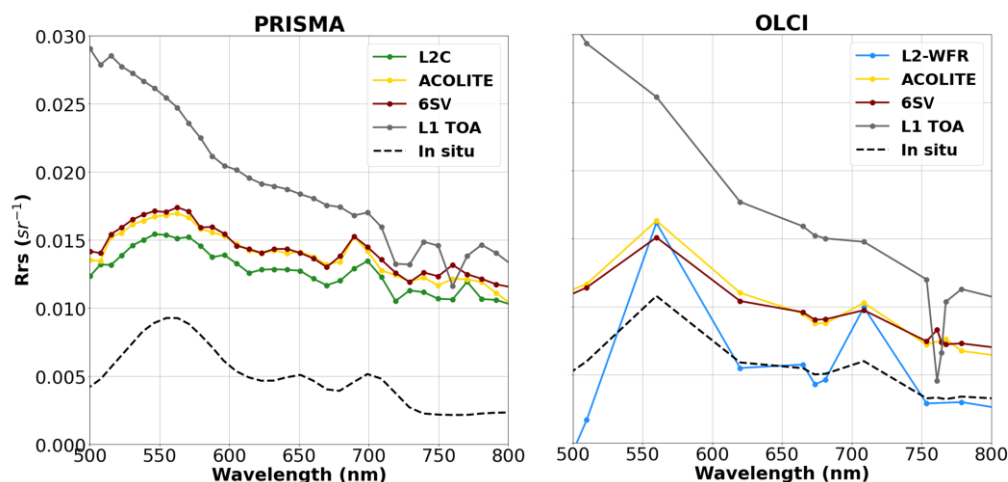


**Figure 2.** Qualitative comparison of in situ  $R_{rs}$  and PRISMA and OLCI AC-corrected  $R_{rs}$  on 3 October 2021 for each atmospheric correction algorithm tested.

For the PRISMA image, the shape similarity can be mainly highlighted by the spectral angle of  $20.21^\circ$  by L2C,  $19.9^\circ$  by ACOLITE, and  $20.22^\circ$  by 6SV, which indicates good proximity between the spectral shapes of in situ measurements and AC models. For ACOLITE and 6SV, more significant differences between in situ  $R_{rs}$  and AC-derived  $R_{rs}$  shapes occur around 700 nm, where a shift in the reflectance peak is observed. In terms of magnitude, the L2C model demonstrated the smallest influence of glint effects, getting closer to the in situ spectrum (Figure 2).

Very similar results were observed for the OLCI image, where 6SV and ACOLITE showed an offset across the spectra, indicating the presence of some residual glint effects. L2-WFR, on the other hand, was not sensitive to the glint effect. For a quantitative investigation into band-wise performance of AC models applied in the OLCI image, the median of bias, RMSE, and MAPE are spectrally presented in Figure 3. As expected, lowest error metrics were observed with L2-WFR model for all OLCI bands, while ACOLITE and 6SV highly overestimated the  $R_{rs}$  values. At the PC absorption band (620 nm), for example, L2-WFR resulted in a bias of 14.9%, while 6SV and ACOLITE errors reached up to 111% and 125%, respectively (Figure 3). Despite the better performance of the OLCI standard product, the L2-WFR AC-corrected spectra showed a pronounced spectral feature in the green and red edge bands (Figure 2), presumably deviating from the in situ  $R_{rs}$  spectra (SA = 20.89%). On the other hand, the SA analysis showed that ACOLITE provided the most similar spectra in comparison with the in situ measurements (SA = 11.22°) and provided products with significantly less noise. Considering that the application of PC models uses math bands as input data, the spectral similarity turns out to be more relevant than the magnitude difference. Therefore, ACOLITE was here considered in applying the models for estimating PC.

Unlike PRISMA images that were also corrected for glint effects, no glint correction model was applied on OLCI images. The spectral range of OLCI bands (400–1020 nm) does not allow the application of WS07 algorithm, which requires the availability of SWIR bands. The decameter-scale of the OLCI sensor imposes challenges on the visual selection of the glint-affected areas in the HED05 model. Furthermore, the push-broom imaging spectrometer of OLCI is tilted off-nadir in a westerly direction by  $12.6^\circ$  in an attempt to mitigate the effects of glint [64]. However, since the application of ACOLITE and 6SV resulted in some spectra magnitude differences, future investigations are necessary to improve  $R_{rs}$  retrieval accuracy.

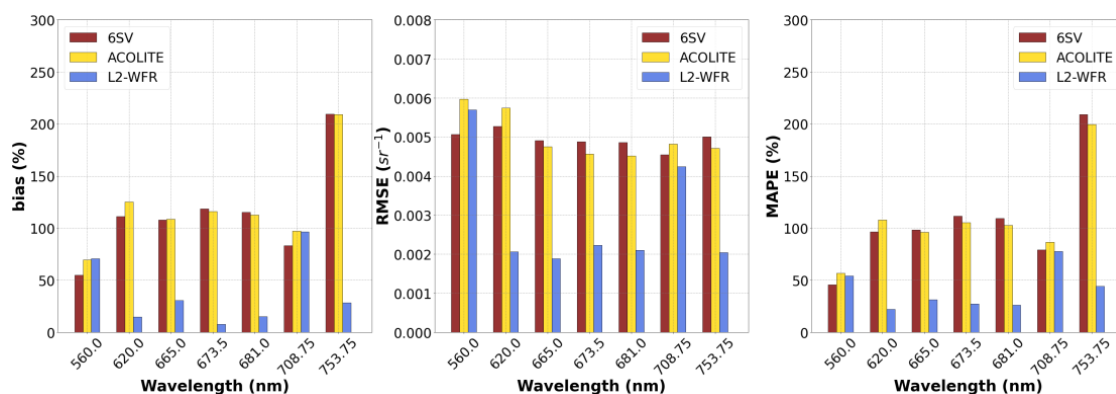


**Figure 3.** Plots of the median spectral statistic (bias, RMSE, and MAPE) for the three AC processors (L2-WFR, 6SV, and ACOLITE) for 3 October 2021 for the most critical wavelengths used in the PC models.

For PRISMA data, on the other hand, three glint-correction approaches were evaluated (WS07, HED05, and KUT09) for each AC method (L2C, ACOLITE, and 6SV). Figure 4 describes the algorithm combination (atmospheric + glint correction methods) performances presenting the scatter plots between modeled and measured  $R_{rs}$ . The median of Bias, RMSE, and MAPE are spectrally presented in Figure 5, where the most critical wavelengths used in the PC retrieval models were highlighted. The best performance for all AC models was achieved in combination with WS07, which shows the potential of exploring SWIR bands in the retrieval of the  $R_{rs}$ . The best combination was obtained by L2C + WS07, where—with the exception of band 563—it presented the smallest errors compared to the other AC processors (Figure 5). Since most bio-optical models that estimate PC apply  $R_{rs}$  mainly around 620 nm, the PRISMA L2C product shows high potential to deliver accurate  $R_{rs}$  products to assess PC concentration. Despite the good performance, hyperspectral sensors present low SNR due to the trade-off between the narrow bandwidth of the spectral channels and the required energy to illuminate detector elements [65]. Recovering the glint effect from noisy SWIR bands might result in uncertainties in the reflectance retrieval. Thus, the band choice used as glint reference is an important factor to be examined before the model application.

Followed by the WS07 model, KUT09 also presented good agreement with the in situ dataset (Figure 4), with better results achieved in combination with 6SV. In combination with the L2C AC processor, the model overestimated the glint effect for all bands (Figure 5). In fact, the KUT09 showed negative  $R_{rs}$  values (gray samples in Figure 4) for all AC processors. These errors might be the result of influence from other components besides glint. The application of HED05 and KUT09 models assumes that the brightness in the NIR region is composed only of sun glint. However, this assumption is not valid for waters optically dominated by phytoplankton where high reflectance values are frequently observed in the NIR [56]. In addition, the adjacency effects are often more expressive in NIR bands. The radiance increment led by adjacent pixels might also overestimate the glint effects in the KUT09 model. Despite these further environmental effects over the NIR bands, the HED05 model presented higher  $R_{rs}$  values for all spectral bands, suggesting an underestimation of the glint effect influence (Figure 4). Indeed, the model did not perform well with any AC processor, with the highest error metrics (Figure 5). The HED05 model requires manually selecting the glinted areas through visual inspection, which can be an important source of error if the selected area is not representative.

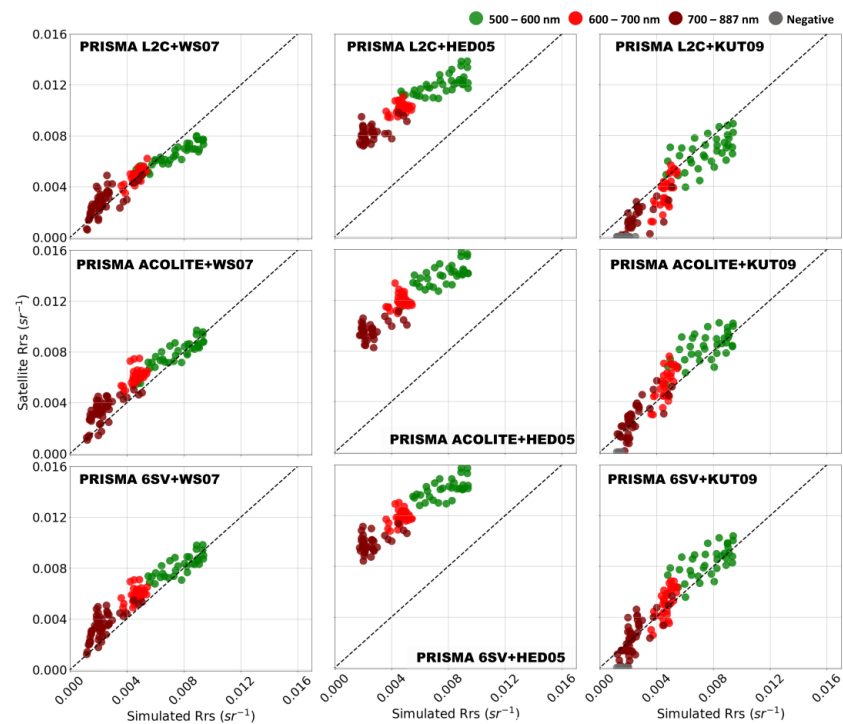


**Figure 4.** Scatterplots of in situ  $R_{rs}$  resampled for PRISMA bands versus estimated PRISMA  $R_{rs}$  for 3 October 2021, using three atmospheric correction algorithms (L2C, ACOLITE, and 6SV) and three glint methods (WS07, HED05, and KUT09) for the 500–885 nm spectral range. A 1:1 line is represented by the dashed line. Negative counts (gray) are plotted as zero.

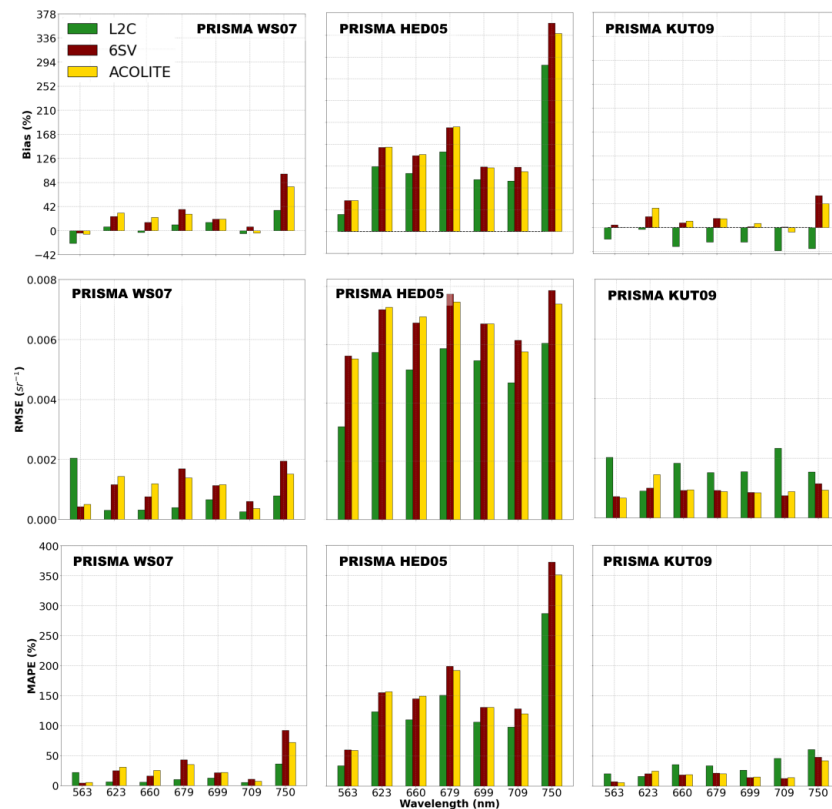


**Figure 5.** Plots of the median spectral statistic (bias, RMSE, and MAPE) for the three glint correction methods (Wang and Shi (2007), Hedley (2005) and Kutser (2009)) for 3 October 2021 for the most critical wavelengths used in the PC models.

## 5.2. Phycocyanin and Chlorophyll-a Algorithm Performance

The results of the modeled PC were compared to reference PC measurements and plotted in Figure 6 with associated error metrics. The dataset was log-transformed in order to reduce the asymmetry of the data distribution [66]. The entire dataset ( $N = 38$  samples) was used to validate the three models considered. Although the SIMIS05 model has been parameterized, the only parameter defined from a direct relationship between the measured and estimated PC concentration was the conversion factor  $\epsilon$ , which was not adapted for Promissão Reservoir. Among the evaluated models to estimate PC concentration, the semi-analytical algorithm (SIMIS05) had the best fit ( $R^2 = 0.94$ ), with the closest linear regression coefficient to unit (slope = 0.75) and the lowest standard error ( $\zeta = 49.56\%$ , MdAE =  $3.06 \text{ mg}\cdot\text{m}^{-3}$ ). The good performance observed evidences the adaptation of the model to the optical conditions of the reservoir. With the exception of  $\epsilon$ , all the other parameters applied were parameterized according to the data collected in situ, which guarantees the good development of the model.

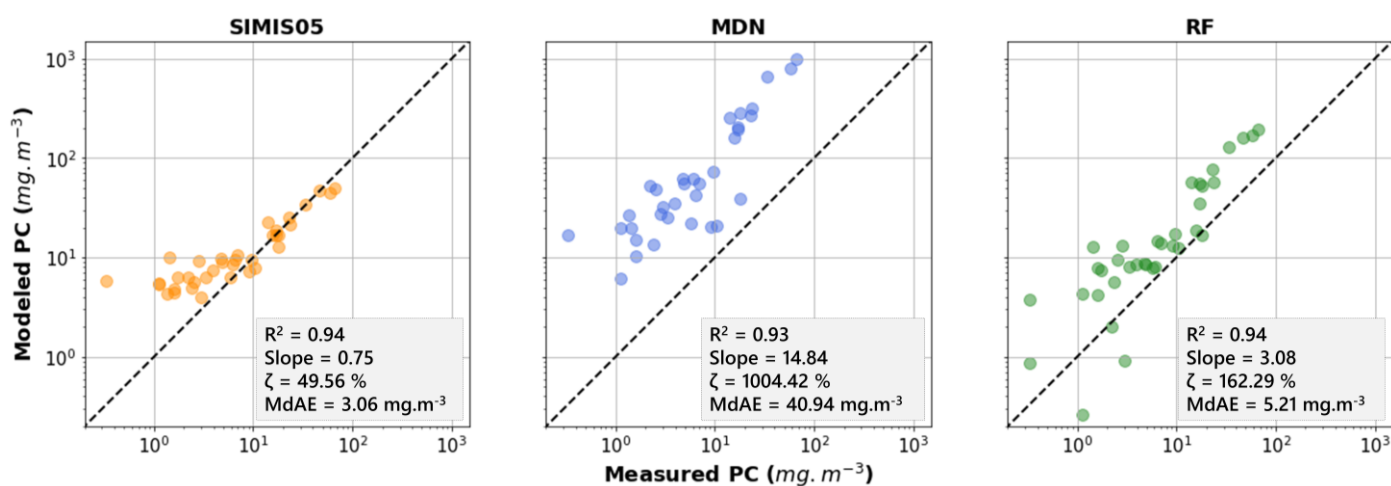


**Figure 6.** Performance assessment of semi-analytical (Simis et al. (2005)) and machine learning algorithms (MDN and RF) using in situ measured PC for 3–10 October 2021. Reported metrics are median symmetric accuracy ( $\zeta$ ), slope, regression coefficient ( $R^2$ ), and the median absolute error (MdAE).

Despite the good performance, the SIMIS05 algorithm showed a tendency to overestimate PC at low concentration ranges. When considering only PC concentrations below  $20 \text{ mg}\cdot\text{m}^{-3}$ , we observed a decrease in the accuracy metrics ( $\zeta = 87.13\%$  and MdAE =  $3.15 \text{ mg}\cdot\text{m}^{-3}$ ) which can be related to the high variation in the  $a_{PC}^*(620)$  for this concentration range. In general,  $a_{PC}^*(620)$  may vary in function of season, cell morphology, pigment composition, changes in nutrients concentration, and light conditions [67]. As reported by Simis et al. [20], the choice of  $a_{PC}^*(620)$  highly affects PC concentration estimates. We considered a unique value of  $a_{PC}^*(620)$  for the whole dataset range, which may have contributed to the increased errors in low pigment concentrations.

Furthermore, estimating low PC in diverse phytoplankton communities has been particularly challenging due to the presence of other optically relevant constituents such as accessory pigments and CDOM. The most commonly influential factor is the dominance of cyanobacteria over the entire phytoplankton biomass, which can be represented by the PC:Chl-a ratio. Li et al. [21] observed for their study area that for PC:Chl-a < 0.5 cyanobacteria were not the dominant species in the water body, which significantly increases the estimative errors. Except for one sample, all other measurements from Promissão Reservoir had PC:Chl-a < 0.5 (Table 1). The lack of spectral dominance of PC and the presence of other optically active constituents that absorb electromagnetic radiation near 620 nm (e.g., Chl-a, Chl-b) might have reduced the accuracy of the parameters used for retrieving PC (e.g.,  $a_{PC}(620)$  in SIMIS05).

Both ML models (MDN and RF) highly overestimated PC values, increasing toward high pigment concentration. Despite that, the coefficients of determination were good for both models ( $R^2_{MDN} = 0.93$  and  $R^2_{RF} = 0.945$ ), where better accuracy was obtained with the RF model ( $\zeta = 162.29\%$  and  $MdAE = 5.21 \text{ mg.m}^{-3}$ ) compared to MDN ( $\zeta = 1004.42\%$  and  $MdAE = 40.94 \text{ mg.m}^{-3}$ ). At low PC concentration ( $<20 \text{ mg.m}^{-3}$ ) an improvement in both models was observed, mainly with the RF ( $\zeta = 132.4\%$  and  $MdAE = 3.98 \text{ mg.m}^{-3}$ ). The RF model was calibrated based on a dataset from Billings Reservoir, which is part of the Tietê Cascade System (Figure 1). The dataset collected at the Billings Reservoir had a similar mean PC:Chl-a (0.14) when compared with Promissão (0.13) which may explain the better performance in comparison with MDN.

MDN, on the other hand, was calibrated using a wider range of water bodies, even though most samples were from few regions worldwide. The lack of samples coming from tropical inland waters might have contributed to reducing the generalization capability of MDN. The training dataset also had a limited number of high PC concentrations ( $>200 \text{ mg.m}^{-3}$ ), which might reduce the ability of MDN to predict accurately in this concentration range (O’Shea et al.) [26]. It was already expected that MDN generalizes best on low PC ( $<20 \text{ mg.m}^{-3}$ ), since it comprises the bulk of the training data. However, the improvement observed for this concentration range was not significant ( $\zeta = 923.46\%$  and  $MdAE = 28.57 \text{ mg.m}^{-3}$  for  $PC < 20 \text{ mg.m}^{-3}$ ). The obtained results suggest that the dataset used for calibrating MDN and RF was not able to capture the relationship between radiometric data and PC concentrations for the Promissão Reservoir. Therefore, the high variability in the performance of ML models outside the areas used for training should be considered when applied for new locations.

Considering Chl-a estimation (Figure 7), both algorithms tested (Gons [58] and MDN) performed with a good correlation with in situ data ( $R^2_{GONS} = 0.798$  and  $R^2_{MDN} = 0.797$ ). Despite that, an overestimation was observed with the Gons model for all dataset ranges ( $MdAE = 42.11 \text{ mg.m}^{-3}$ ). Contrary to the PC estimation, the MDN model performed well in Chl-a estimation at low and high pigment concentrations ( $\zeta = 47.88\%$  and  $MdAE = 23.21 \text{ mg.m}^{-3}$ ).

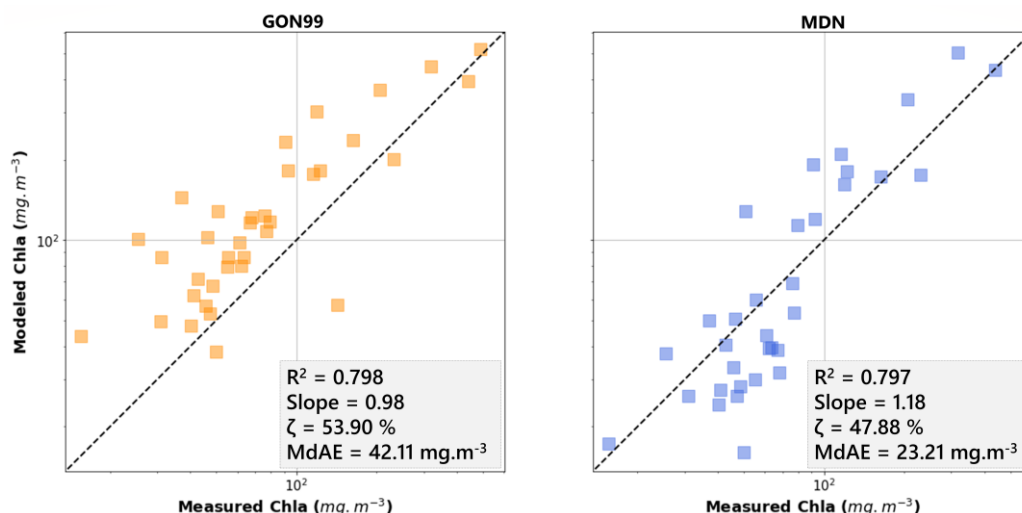


**Figure 7.** Performance assessment of semi-analytical (Gons [58]) and machine learning algorithms (MDN) using in situ measured Chl-a for 3rd–10th, October, 2021. Reported metrics are median symmetric accuracy ( $\zeta$ ), slope, regression coefficient ( $R^2$ ), and the median absolute error (MdAE).

### 5.3. Mapping PC: Model Assessment on Satellite Observations

Figure 8 shows PC concentration mapped with the three assessed models applied to the PRISMA data corrected using the L2C+WS07 combination. Considering the matchup samples between the in situ measurements and OLCI/PRISMA overpass ( $N = 4$ ), comparisons between the satellite-estimated PC against PC in situ measurements are shown in Table 5. For the PRISMA image, the spatial distribution of the predicted values was

similar for all methods, where higher PC concentrations are observed in the main river (Figure 8). However, the magnitude of the estimates varied substantially. Following the in situ results, all models overestimated the PC concentrations (Table 5), especially MDN, which presented the worst MdAE ( $23.58 \text{ mg}\cdot\text{m}^{-3}$ ). The best performance for the PRISMA image was achieved by the SIMIS05 model ( $\text{MdAE} = 3.18 \text{ mg}\cdot\text{m}^{-3}$ ), which—based on the significant improvement in the PC estimates (Table 5)—was used in the assessment of the OLCI image, ensuring consistency between both satellites (Figure 9). The pigment concentration from the multispectral sensor is also showed in Table 5.

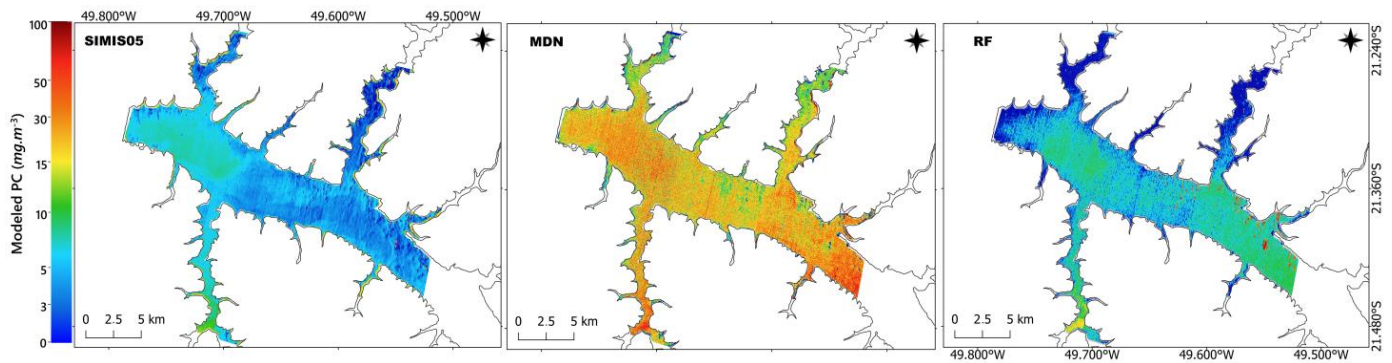


**Figure 8.** PC product maps of Promissão Reservoir on 3 October 2021 produced by the Simis et al. (2005) model and ML algorithms (MDN and RF) applied on the PRISMA L2C+WS07 image.

**Table 5.** In situ measured PC ( $\text{mg}\cdot\text{m}^{-3}$ ) compared against retrieved PC ( $\text{mg}\cdot\text{m}^{-3}$ ) from PRISMA and OLCI images for 3 October 2021. The spatial distribution of the labeled stations is shown in Figure 9.

Station	In Situ	PRISMA			OLCI
		SIMIS05	MDN	RF	SIMIS05
P07	1.12	4.69	24.46	6.23	5.17
P08	1.12	3.89	38.68	5.09	4.93
P09	0.33	4.12	24.16	8.65	4.57
P01	3.33	4.07	24.97	9.05	4.69

The PC mapping from OLCI/ACOLITE images (Figure 9) agreed with PRISMA PC using the SIMIS05 model, with an  $\text{MdAE} = 3.93 \text{ mg}\cdot\text{m}^{-3}$ . The PC estimated values (Table 5) indicated a good performance of the parameterized SIMIS05 model applied in a multispectral sensor with medium spatial resolution, even at low PC concentrations. In general, the behavior of the estimated PC from satellite imagery was expected considering the previous in situ analysis and the concentration range of the matchup samples ( $0.33\text{--}3.33 \text{ mg}\cdot\text{m}^{-3}$ ). The observed errors might result from spatial and temporal misalignment between the in situ measured and remotely estimated PC. Variations in the surface cyanobacteria concentration can occur during the time window between field sampling and imaging [19]. Furthermore, the vertical structure of the cyanobacterial bloom and dominant species can vary spatially and temporally, which affects the signal used for PC retrieval. Thus, spatial scale and temporal misalignment can result in large differences in the in situ measured and remotely estimated PC.

In addition, another important source of error is related to the  $R_{rs}$  uncertainty [20]. It is well known that imperfect correction of the atmospheric effects can result in further inaccuracies in the retrieved product, depending on the sensitivity of the retrieval algorithms [68]. The AC analysis demonstrated some limitation in the AC processor models, mainly in the blue–green wavelengths. In this sense, the use of shape-based algorithms can reduce the uncertainties derived from the atmospheric noise. O’Shea et al. [26] assess the impact of  $R_{rs}$  uncertainties on PC retrieval accuracy and demonstrated that the combined

used of the MDN model with BRs and LHs produces high-accuracy results for regions with low PC, despite the presence of  $R_{rs}$  uncertainties. Although the ML (RF and MDN) and SIMIS05 model do not use the pure spectral bands, investigations of the impact of satellite  $R_{rs}$  uncertainties on PC estimates are essential to minimize the propagation of errors.

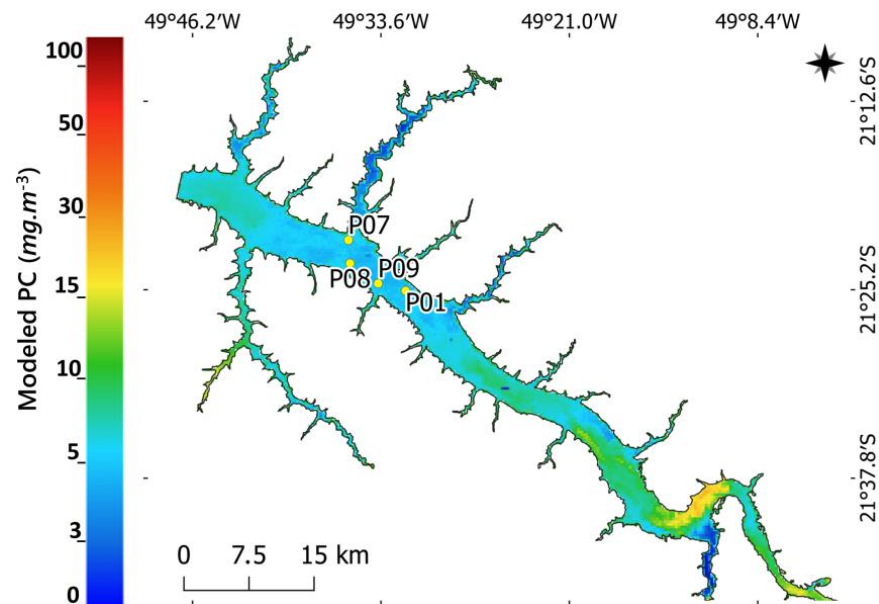


**Figure 9.** PC product map using SIMIS05 model in OLCI (AC-corrected using ACOLITE) image on 3 October 2021, with associated in situ matchup points (labels which match with in situ concentrations Table 5).

Further comparisons between PRISMA (L2C+WS07) and OLCI (ACOLITE) PC product maps are shown in Figure 10. For each considered date, co-located Regions of Interest (ROI) were randomly selected in both PRISMA and OLCI images, and the PC concentration estimate from each sensor was compared (Table 6). In order to assess the impact of the different spatial resolution of PRISMA (30 m) and OLCI (300 m), the single pixel values of each image were directly used in the comparisons without any resampling step. Despite the difference in the spatial resolution between OLCI and PRISMA, the visual inspection of the maps conveys an intuitively good agreement among the two sensors. The differences between the PC concentration from PRISMA and OLCI were, in general, on the order of  $\sim 2 \text{ mg.m}^{-3}$  (Table 6). For both dates, higher differences in the pigment concentration occurred in pixels with small bloom spots (R5 at 4 September 2021 and R2 at 26 July 2022) that were not detected in the OLCI images. In fact, the 30 m spatial resolution of PRISMA allows for a finer spatial distribution of the pigment concentration, particularly along the tributaries of rivers (reduced flooded areas) and discrete spots of blooms (high spatial frequency within small areas).

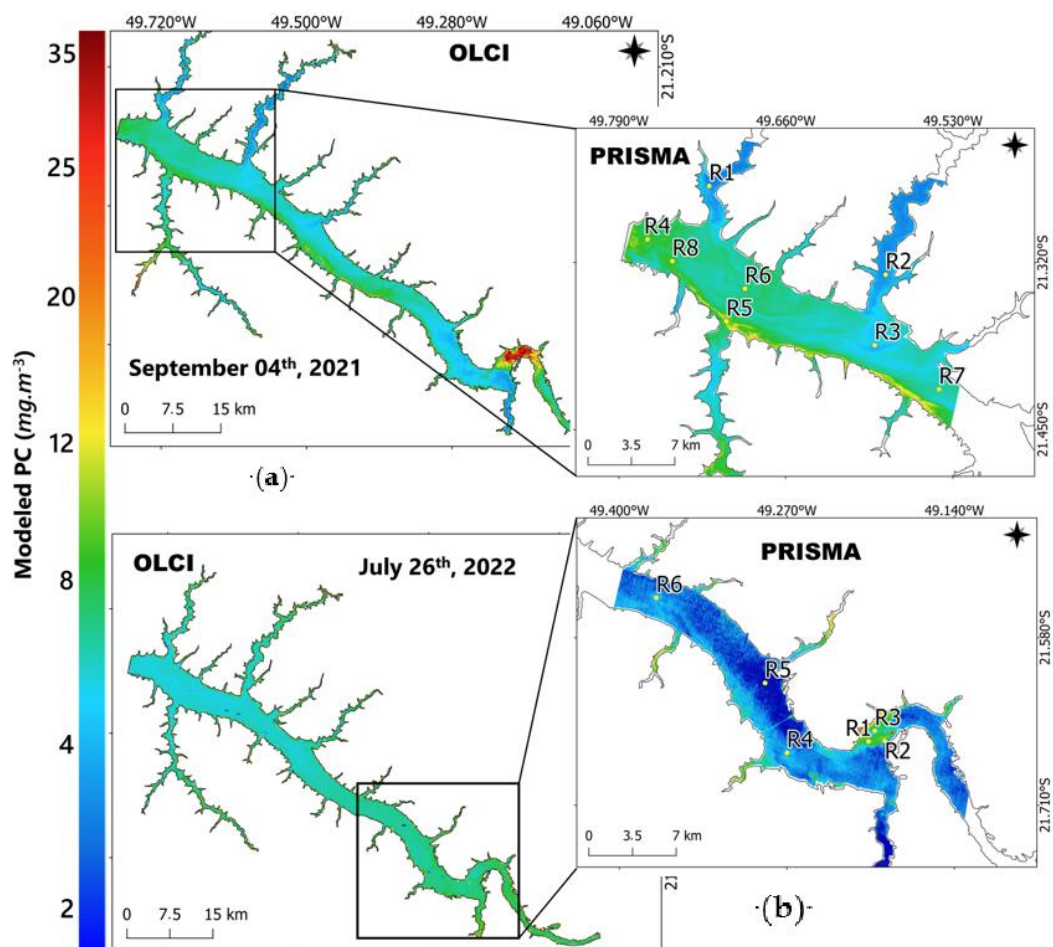


**Figure 10.** Comparison between OLCI (AC-corrected using ACOLITE) and PRISMA PC product maps using SIMIS05 model in Promissão Reservoir for (a) 4 September 2021 and (b) 26 July 2022.

**Table 6.** Comparison between SIMIS05-retrieved PC ( $\text{mg}\cdot\text{m}^{-3}$ ) from PRISMA and OLCI images. The spatial distribution of the labeled stations is shown in Figure 10. The station highlighted in green indicates the presence of bloom spots.

4 September 2021			26 July 2022		
ROI	PRISMA	OLCI	ROI	PRISMA	OLCI
R01	2.42	3.32	R01	7.15	5.45
R02	2.73	3.06	R02	25.52	7.42
R03	3.36	3.99	R03	4.20	5.56
R04	7.98	6.92	R04	4.76	6.14
R05	10.27	6.51	R05	0.85	6.52
R06	6.57	5.60	R06	3.52	5.91
R07	5.64	5.21	-	-	-
R08	8.17	6.64	-	-	-

## 6. Conclusions

Although different studies reveal the potential of PC as a proxy for cyanobacteria biomass, monitoring this pigment from space is limited by the availability of a spectral band centered near 620 nm. In this context, the capacity of hyperspectral sensors in measuring across the full VNIR spectrum allows the optical constituents present in water bodies to be better estimated [69,70]. However, the uncertainties in the hyperspectral

reflectance resulting from instrument noise and the atmospheric correction process can propagate to errors in the retrieved satellite products. These effects still require an amount of investigation in order to minimize the uncertainty propagation. In this study, we conducted preliminary analysis of water reflectance derived from PRISMA hyperspectral sensors in a Brazilian reservoir. Above-water in situ reflectance were used to evaluate different atmospheric and glint-correction models. We also evaluated different models (semi-analytical and ML) for PC estimation. Among the AC models tested in the PRISMA image, L2C PRISMA products presented a better spectral similarity with the in situ data in the presence of glint. This is an important finding, since ACOLITE and 6SV have to be performed by the user and still require prior knowledge of atmospheric parameters that directly affect the performance of the model, as is the case of the 6SV. In the case of OLCI, although the L2 standard processor presented the best performance in the presence of glint, higher differences were observed in the spectra shape (mainly in the green and red peaks), which directly affects the accuracy of shape-based algorithms.

Regarding the application of glint correction in the PRISMA image, the best achievements with an AC algorithm were derived from the Wang and Shi [53] model in combination with L2C. The ASI product has shown high potential to deliver accurate BOA reflectance products, especially in the visible region. In addition, the PRISMA sensor provides measurements in the SWIR part of the spectrum which could relieve some previous assumptions made for the NIR part of the spectrum. First, absorption of water molecules is more pronounced in the SWIR than in the NIR wavelength range by more than one order of magnitude, thereby reinforcing the assumption of 'black water' in the SWIR. Secondly, the atmosphere is more transparent with a weak amount of diffuse light (i.e., lower contribution of aerosols and air molecules), making measurements more sensitive to the glint contribution at such wavelengths [71]. As a result, 'deglinting' methods could be potentially improved based on the exploitation of the SWIR data. Despite the promising results, the matchup analysis presented in this study is very limited, requiring further studies to confirm our results and extend performance analysis to other optical water types with a wider range of PC concentration. Furthermore, a robust method for retrieving atmospheric aerosol load for AC is still one of the biggest challenges of remote sensing in productive inland waters, and further studies are still needed to understand the impact of these uncertainties in pigment estimation.

The performances of two algorithms approaches (semi-analytical and ML) for retrieval PC were tested considering a dataset of pigment radiometric data collected in a Brazilian reservoir, and the effects of several potential sources of error were analyzed. These error sources include instrumental error, measurement methodology, satellite  $R_{rs}$  uncertainties derived from atmospheric noise, and the presence of pigments with overlapping light-absorption features. The nested semi-analytical model of Simis et al. [22] gave the best fit and accuracy for all concentration ranges, different from the ML models that significantly overestimated the pigment concentration. Our findings suggest that these errors could be markedly reduced by using site-specific adaptations of each model.

Finally, the comparisons between OLCI and PRISMA PC maps derived from Simis et al. [22] show good agreement, with the advantage of PRISMA being the detection of smaller spatial variations. Despite the spatial resolution of OLCI being one order of magnitude lower than PRISMA, its high revisit time always ensured a matchup, while providing 15 spectral bands potentially matching those of PRISMA. In fact, the synergic use of different sensors could improve the temporal analyses that are useful to understand, for example, cyanobacteria dynamics.

**Author Contributions:** Conceptualization, T.M.A.d.L., C.G., M.B. and C.C.F.B.; methodology, T.M.A.d.L., A.F., A.P. and F.N.B.; software, T.M.A.d.L., A.F., A.P. and F.N.B.; validation, T.M.A.d.L.; formal analysis, T.M.A.d.L., C.G., M.B., C.C.F.B., A.F., A.P. and F.N.B.; investigation, T.M.A.d.L., C.G., M.B., C.C.F.B., A.F., A.P. and F.N.B.; resources, C.G., M.B. and C.C.F.B.; writing—original draft preparation, T.M.A.d.L.; writing—review and editing, C.G., M.B., C.C.F.B., A.F., A.P. and F.N.B.; supervision, C.G., M.B. and C.C.F.B. All authors have read and agreed to the published version of the manuscript.

**Funding:** This research was funded by H2020 PrimeWater, grant number 870497; H2020 Water-ForCE, grant number 101004186; São Paulo Research Foundation (FAPESP), grant number 2022/01107-2; and FAPESP, grant number 2020/14613-8.

**Data Availability Statement:** The scripts for running the AC with the 6SV code, and the scripts to adapt SIMIS05 algorithm to the study area, are available via <https://github.com/thaimunhoz/prisma-olci-paper> (accessed on 14 January 2023), along with additional statistical scripts used in this paper.

**Acknowledgments:** We thank the anonymous Remote Sensing reviewers for the careful suggestions that helped to improve this work.

**Conflicts of Interest:** The authors declare no conflict of interest.

## References

1. Miola, A.; Schiltz, F. Measuring sustainable development goals performance: How to monitor policy action in the 2030 Agenda implementation? *Ecol. Econ.* **2019**, *164*, 106379. [[CrossRef](#)] [[PubMed](#)]
2. Azevedo, S.M.F.O.; Vasconcelos, V.M. Toxinas de cianobactérias: Causas e Consequências para a saúde pública. In *Ecotoxicologia Aquática: Princípios e Aplicações*, 1st ed.; Zagatto, P.A., Bertoletti, E., Eds.; Rima: Rio de Janeiro, Brazil, 2006; pp. 433–452.
3. Giuliani, G.; Nativi, S.; Obregon, A.; Beniston, M.; Lehmann, A. Spatially enabling the Global Framework for Climate Services: Reviewing geospatial solutions to efficiently share and integrate climate data & information. *Clim. Serv.* **2017**, *8*, 44–58. [[CrossRef](#)]
4. Lehmann, A.; Chaplin-Kramer, R.; Lacayo, M.; Giuliani, G.; Thau, D.; Koy, K.; Goldberg, G.; Sharp, R., Jr. Lifting the Information Barriers to Address Sustainability Challenges with Data from Physical Geography and Earth Observation. *Sustainability* **2017**, *9*, 858. [[CrossRef](#)]
5. Shi, K.; Zhang, Y.; Qin, B.; Zhou, B. Remote sensing of cyanobacterial blooms in inland waters: Present knowledge and future challenges. *Sci. Bull.* **2019**, *64*, 1540–1556. [[CrossRef](#)]
6. Coffey, M.M.; Schaeffer, B.A.; Foreman, K.; Porteous, A.; Loftin, K.A.; Stumpf, R.P.; Darling, J.A. Assessing cyanobacterial frequency and abundance at surface waters near drinking water intakes across the United States. *Water Res.* **2021**, *201*, 117377. [[CrossRef](#)]
7. Schaeffer, B.A.; Urquhart, E.; Coffey, M.; Salls, W.; Stumpf, R.P.; Loftin, K.A.; Werdell, P.J. Satellites quantify the spatial extent of cyanobacterial blooms across the United States at multiple scales. *Ecol. Indic.* **2022**, *140*, 108990. [[CrossRef](#)]
8. Jang, M.T.G.; Alcântara, E.; Rodrigues, T.; Park, E.; Ogashawara, I.; Marengo, J.A. Increased chlorophyll-a concentration in Barra Bonita reservoir during extreme drought periods. *Sci. Total Environ.* **2022**, *843*, 157106. [[CrossRef](#)]
9. Ogashawara, I. Determination of phycocyanin from space—A bibliometric analysis. *Remote Sens.* **2020**, *12*, 567. [[CrossRef](#)]
10. Pahlevan, N.; Smith, B.; Schalles, J.; Binding, C.; Cao, Z.; Ma, R.; Stumpf, R. Seamless retrievals of chlorophyll-a from Sentinel-2 (MSI) and Sentinel-3 (OLCI) in inland and coastal waters: A machine-learning approach. *Remote Sens. Environ.* **2020**, *240*, 111604. [[CrossRef](#)]
11. Dierssen, H.M. Realizing the potential of hyperspectral remote sensing in coastal and inland waters. In Proceedings of the IEEE International Geoscience and Remote Sensing Symposium IGARSS, Brussels, Belgium, 11–16 July 2021. [[CrossRef](#)]
12. Karger-Muller, F.E.; Hestir, E.; Ade, C.; Turpie, K.; Roberts, D.A.; Siegel, D.; Miller, R.J.; Humm, D.; Izenberg, N.; Keller, M.; et al. Satellite sensor requirements for monitoring essential biodiversity variables of coastal ecosystems. *Ecol. Appl.* **2018**, *28*, 749–760. [[CrossRef](#)]
13. Ahn, C.Y.; Joung, S.H.; Yoon, S.K.; Oh, H.M. Alternative alert system for cyanobacterial bloom, using phycocyanin as level determinant. *J. Microbiol.* **2007**, *45*, 98–104. [[PubMed](#)]
14. Augusto-Silva, P.B.; Ogashawara, I.; Barbosa, C.C.; De Carvalho, L.A.S.; Jorge, D.S.F.; Fornari, C.I.; SteCH, J. Analysis of MERIS Reflectance Algorithms for Estimating Chlorophyll-a Concentration in a Brazilian Reservoir. *Remote Sens.* **2014**, *6*, 11689–11707. [[CrossRef](#)]
15. Watanabe, F.S.Y.; Alcântara, E.; Rodrigues, T.W.P.; Imai, N.N.; Barbosa, C.C.F.; Rotta, L.H.S. Estimation of chlorophyll-a concentration and the trophic state of the Barra Bonita Hydroelectric Reservoir using OLI/Landsat-8 images. *Int. J. Environ. Res. Public Health* **2015**, *12*, 10391–10417. [[CrossRef](#)] [[PubMed](#)]
16. Cairo, C.; Barbosa, C.C.F.; Lobo, F.L.; Novo, E.M.L.M. Hybrid Chlorophyll-a Algorithm for Assessing Trophic States of a Tropical Brazilian Reservoir Based on MSI/Sentinel-2 Data. *Remote Sens.* **2020**, *12*, 40. [[CrossRef](#)]
17. Dekker, A.G. Detection of Optical Water Quality Parameters for Eutrophic Waters by High Resolution Remote Sensing. Ph.D. Thesis, Doctorate in Research and graduation internal—Vrije University, Amsterdam, The Netherlands, 1993.
18. Schalles, J.F.; Yacobi, Y.Z. Remote detection and seasonal patterns of phycocyanin, carotenoid and chlorophyll pigments in eutrophic waters. *Arch. Fur Hydrobiol.* **2000**, *55*, 153–168. [[CrossRef](#)]
19. Kutser, T. Quantitative detection of chlorophyll in cyanobacterial blooms by satellite remote sensing. *Limnol. Oceanogr.* **2004**, *49*, 2179–2189. [[CrossRef](#)]
20. Simis, S.G.H.; Ruiz-Verdu, A.; Dominguez-Gomez, J.A.; Pena-Martinez, R.; Peters, S.W.M.; Gons, H.J. Influence of phytoplankton pigment composition on remote sensing of cyanobacterial biomass. *Remote Sens. Environ.* **2007**, *106*, 414–427. [[CrossRef](#)]

21. Li, L.; Li, L.; Song, K. Remote sensing of freshwater cyanobacteria: An extended IOP Inversion Model of Inland Waters (IIMIWI) for partitioning absorption coefficient and estimating phycocyanin. *Remote Sens. Environ.* **2015**, *157*, 9–23. [[CrossRef](#)]
22. Simis, S.G.H.; Peters, S.W.M.; Gons, H.J. Remote sensing of the cyanobacterial pigment phycocyanin in turbid inland water. *Limnol. Oceanogr.* **2005**, *50*, 237–245. [[CrossRef](#)]
23. Ruiz-Verdú, A.; Simis, S.G.H.; de Hoyos, C.; Gons, H.J.; Peña-Martínez, R. An evaluation of algorithms for the remote sensing of cyanobacterial biomass. *Remote Sens. Environ.* **2008**, *112*, 3996–4008. [[CrossRef](#)]
24. Yan, Y.; Bao, Z.; Shao, J. Phycocyanin concentration retrieval in inland waters: A comparative review of the remote sensing techniques and algorithms. *J. Great Lakes Res.* **2018**, *44*, 748–755. [[CrossRef](#)]
25. Riddick, C.A.L.; Hunter, P.D.; Domínguez-Gómez, J.A.; Martínez-Vicente, V.; Présing, M.; Horváth, H.; Kovács, A.W.; Vörös, L.; Zsigmond, E.; Tyler, A.N. Optimal Cyanobacterial Pigment Retrieval from Ocean Colour Sensors in a Highly Turbid, Optically Complex Lake. *Remote Sens.* **2019**, *11*, 1613. [[CrossRef](#)]
26. O’shea, R.E.; Pahlevan, N.; Smith, B.; Bresciani, M.; Egerton, T.; Giardino, C.; Li, L.; Moore, T.; Ruiz-Verdu, A.; Ruberg, S.; et al. Advancing cyanobacteria biomass estimation from hyperspectral observations: Demonstrations with HICO and PRISMA imagery. *Remote Sens. Environ.* **2021**, *266*, 112693. [[CrossRef](#)]
27. Braga, F.; Fabbretto, A.; Vanhellemont, Q.; Bresciani, M.; Giardino, C.; Scarpa, G.M.; Manfè, G.; Concha, J.A.; Brando, V.E. Assessment of PRISMA water reflectance using autonomous hyperspectral radiometry. *ISPRS J. Photogramm. Remote Sens.* **2022**, *192*, 99–114. [[CrossRef](#)]
28. Niroumand-Jadidi, M.; Bovolo, F.; Bruzzone, L. Water quality retrieval from PRISMA Hyperspectral images: First experience in a turbid lake and comparison with Sentinel-2. *Remote Sens.* **2020**, *12*, 3984. [[CrossRef](#)]
29. Bresciani, M.; Giardino, C.; Fabbretto, A.; Pellegrino, A.; Mangano, S.; Free, G.; Pinardi, M. Application of new hyperspectral sensors in the remote sensing of aquatic ecosystem health: Exploiting PRISMA and DESIS for four Italian lakes. *Resources* **2022**, *11*, 8. [[CrossRef](#)]
30. Borfecchia, F.; Micheli, C.; De Cecco, L.; Sannino, G.; Struglia, M.V.; Di Sarra, A.G.; Mattiazzo, G. Satellite multi/hyper spectral HR sensors for mapping the *Posidonia oceanica* in south mediterranean islands. *Sustainability* **2021**, *13*, 13715. [[CrossRef](#)]
31. Cogliati, S.; Sarti, F.; Chiarantini, L.; Cosi, M.; Lorusso, R.; Lopinto, E.; Colombo, R. The PRISMA imaging spectroscopy mission: Overview and first performance analysis. *Remote Sens. Environ.* **2021**, *262*, 112499. [[CrossRef](#)]
32. Vanhellemont, Q. Adaptation of the dark spectrum fitting atmospheric correction for aquatic applications of the Landsat and Sentinel-2 archives. *Remote Sens. Environ.* **2019**, *225*, 175–192. [[CrossRef](#)]
33. Vermote, E.; Tanre, D.; Deuze, J.L.; Herman, M.; Morcrette, J.J.; Kotchenova, S.Y. Second simulation of a satellite signal in the solar spectrum, 6S: An overview. *IEEE Trans. Geosci. Remote Sens.* **1997**, *35*, 675–686. [[CrossRef](#)]
34. Barbosa, C.C.F.; Novo, E.M.L.M.; Martins, V.S. *Introdução ao Sensoriamento Remoto de Sistemas Aquáticos: Princípios e Aplicações*, 1st ed.; INPE: São José dos Campos, Brazil, 2019; 178p, ISBN 978-85-17-0009-9.
35. Bernardo, N.; Alcântara, E.; Watanabe, F.; Rodrigues, T.; Carmo, A.; Gomes, A.; Andrade, C. Glint removal assessment to estimate the remote sensing reflectance in inland waters with widely differing optical properties. *Remote Sens.* **2018**, *10*, 1655. [[CrossRef](#)]
36. Mobley, C.D. Estimation of the remote-sensing reflectance from above-surface measurements. *Appl. Opt.* **1999**, *38*, 7442–7455. [[CrossRef](#)] [[PubMed](#)]
37. Mueller, J.L.; Austin, R.W. SeaWiFS Technical Report Series. *NASA Tech. Memo.* **1995**, *25*.
38. Kutser, T.; Vahtmae, E.; Paavel, B.; Kauer, T. Removing glint effects from field radiometry data measured in optically complex coastal and inland waters. *Remote Sens. Environ.* **2013**, *113*, 85–89. [[CrossRef](#)]
39. Pelloquin, C.; Nieke, J. Sentinel-3 OLCI and SLSTR simulated spectral response function. *Tech. Note* **2012**, *1*, S3-TN-ESA-PL-316. [[CrossRef](#)]
40. Tassan, S.; Ferrari, G.M. A sensitivity analysis of the ‘Transmittance-Reflectance’ method for measuring light absorption by aquatic particles. *J. Plankton Res.* **2002**, *24*, 757–774. [[CrossRef](#)]
41. Roesler, C.S. Theoretical and experimental approaches to improve the accuracy of particulate absorption coefficients derived from the quantitative filter technique. *Limnol. Oceanogr.* **2003**, *43*, 1649–1660. [[CrossRef](#)]
42. Stramski, D.; Reynolds, R.A.; Kaczmarek, S.; Uitz, J.; Zheng, G. Correction of pathlength amplification in the filter-pad technique for measurements of particulate absorption coefficient in the visible spectral region. *Appl. Opt.* **2015**, *54*, 6763–6782. [[CrossRef](#)]
43. APHA. *Standard Methods for the Examination of Water and Wastewater*, 20th ed.; American Public Health Association: Washington, DC, USA, 1998; 874p.
44. Sarada, R.; Pillai, M.G.; Ravishankar, G.A. Phycocyanin from *Spirulina* sp: Influence of processing of biomass on phycocyanin yield, analysis of efficacy of extraction methods and stability studies on phycocyanin. *Process Biochem.* **1999**, *34*, 795–801. [[CrossRef](#)]
45. Horváth, H.; Kovács, A.W.; Riddick, C.; Présing, M. Extraction methods for phycocyanin determination in freshwater filamentous cyanobacteria and their application in a shallow lake. *Eur. J. Phycol.* **2013**, *48*, 278–286. [[CrossRef](#)]
46. Bennett, A.; Bogorad, L. Complementary chromatic adaptation in a filamentous blue-green alga. *J. Cell Biol.* **1973**, *58*, 419–435. [[CrossRef](#)] [[PubMed](#)]
47. Giardino, C.; Bresciani, M.; Braga, F.; Fabbretto, A.; Ghirardi, N.; Pepe, M.; Gianinetto, M.; Colombo, R.; Cogliati, S.; Ghebrehiwot, S.; et al. First evaluation of PRISMA Level 1 data for water applications. *Sensors* **2020**, *20*, 4553. [[CrossRef](#)] [[PubMed](#)]

48. ESA. Sentinel-Online: Product Types Information. Available online: <https://sentinels.copernicus.eu/web/sentinel/user-guides/sentinel-3-olci/product-types> (accessed on 22 November 2022).
49. Ouaidrari, H.; Vermote, E.F. Operational atmospheric correction of Landsat TM data. *Remote Sens. Environ.* **1999**, *70*, 4–15. [[CrossRef](#)]
50. ASI. PRISMA Products Specification Document. Issue 2.3. Available online: [http://prisma.asi.it/missionselect/docs/PRISMA%20Product%20Specifications\\_Is2\\_3.pdf](http://prisma.asi.it/missionselect/docs/PRISMA%20Product%20Specifications_Is2_3.pdf) (accessed on 24 October 2022).
51. Renosh, P.R.; Doxaran, D.; Keukelaere, L.; GOSSN, J.I. Evaluation of atmospheric correction algorithms for Sentinel-2-MSI and Sentinel-3-OLCI in highly turbid estuarine waters. *Remote Sens.* **2020**, *12*, 1285. [[CrossRef](#)]
52. Wilson, R.T. Py6S: A Python interface to the 6S radiative transfer model. *Comput. Geosci.* **2013**, *51*, 166–171. [[CrossRef](#)]
53. Wang, M.; Shi, W. The NIR-SWIR combined atmospheric correction approach for MODIS ocean color data processing. *Opt. Express* **2007**, *15*, 15722–15733. [[CrossRef](#)]
54. Gao, B.-C.; Montes, M.J.; Davis, C.O.; Goetz, A.F.H. Atmospheric correction algorithms for hyperspectral remote sensing data of land and ocean. *Remote Sens. Environ.* **2009**, *113*, 2017–2224. [[CrossRef](#)]
55. Hedley, J.D.; Harbone, A.R.; Mumby, P.J. Simple and robust removal of sun glint for mapping shallow-water benthos. *Int. J. Remote Sens.* **2005**, *26*, 2107–2112. [[CrossRef](#)]
56. Kutser, T.; Vahtmae, E.; Praks, J. A sun glint correction method for hyperspectral imagery containing areas with non-negligible water leaving NIR signal. *Remote Sens. Environ.* **2009**, *113*, 2267–2274. [[CrossRef](#)]
57. Gordon, H.R.; Brown, O.B.; Jacobs, M.M. Computed relationships between the inherent and apparent optical properties of a flat homogeneous ocean. *Appl. Opt.* **1975**, *14*, 417–427. [[CrossRef](#)]
58. Gons, H.J. Optical Teledetection of Chlorophyllain Turbid Inland Waters. *Environ. Sci. Technol.* **1999**, *33*, 1127–1132. [[CrossRef](#)]
59. Begliomini, F.N. Cyanobacteria Monitoring on Urban Reservoir Using Hyperspectral Orbital Remote Sensing Data and Machine Learning. Ph.D. Thesis, Master in Remote Sensing—Instituto Nacional de Pesquisas Espaciais (INPE), São José dos Campos, Brazil, 2022.
60. Hunter, P.D.; Tyler, A.N.; Carvalho, L.; Codd, G.A.; Marberly, S.C. Hyperspectral remote sensing of cyanobacterial pigments as indicators for cell populations and toxins in eutrophic lakes. *Remote Sens. Environ.* **2010**, *114*, 2705–2718. [[CrossRef](#)]
61. Mishra, S.; Mishra, D.R. A novel remote sensing algorithm to quantify phycocyanin in cyanobacterial algal blooms. *Environ. Res. Lett.* **2014**, *9*, 114003. [[CrossRef](#)]
62. Mishra, S.; Mishra, D.R. Normalized difference chlorophyll index: A novel model for remote estimation of chlorophyll-a concentration in turbid productive waters. *Remote Sens. Environ.* **2012**, *117*, 394–406. [[CrossRef](#)]
63. Morley, S.K.; Britto, T.V.; Walling, D.T. Measures of model performance based on the log accuracy ratio. *Space Weather* **2018**, *16*, 69–88. [[CrossRef](#)]
64. Kravitz, J.; Matthews, M.; Bernard, S.; Griffith, D. Application of Sentinel 3 OLCI for chl-a retrieval over small inland water targets: Successes and challenges. *Remote Sens. Environ.* **2020**, *237*, 111562. [[CrossRef](#)]
65. Moses, J.W.; Steckx, S.; Montes, M.J.; Keukelaere, L.D.; Knaeps, E. Atmospheric Correction for Inland Waters. In *Bio-Optical Modeling and Remote Sensing of Inland Waters*, 1st ed.; Mishra, D.R., Ogashawara, I., Gitelson, A.A., Eds.; Elsevier: Amsterdam, The Netherlands, 2017; 334p, ISBN 978-0-12-804644-9.
66. Qiang, Y.; Xindong, W. 10 Challenging problems in data mining research. *Int. J. Inf. Technol. Decis. Mak.* **2006**, *5*, 597–604.
67. Simis, S.G.H.; Kauko, H.M. In vivo mass-specific absorption spectra of phycobilin pigments through selective bleaching. *Limnol. Oceanogr. Methods* **2012**, *10*, 214–226. [[CrossRef](#)]
68. Moses, W.J.; Bowles, J.H.; Lucke, R.L.; Corsor, M.R. Impact of signal-to-noise ratio in a hyperspectral sensor on the accuracy of biophysical parameter estimation in case II waters. *Opt. Express* **2012**, *20*, 4309–4330. [[CrossRef](#)]
69. Giardino, C.; Brando, V.E.; Gege, P.; Pinnel, N.; Hochberg, E.; Knaeps, E.; Reusen, I.; Doerffer, R.; Bresciani, M.; Braga, F.; et al. Imaging spectrometry of inland and coastal waters: State of the art, achievements and perspectives. *Surv. Geophys.* **2019**, *40*, 401–429. [[CrossRef](#)]
70. Dierssen, H.M.; Ackleson, S.G.; Joyce, K.E.; Hestir, E.L.; Castagna, A.; Lavender, S.; Mcmanus, M.A. Living up to the hype of hyperspectral aquatic remote sensing: Science, resources and outlook. *Front. Environ. Sci.* **2021**, *9*. [[CrossRef](#)]
71. Harmel, T.; Chami, M.; Tormos, T.; Reynaud, N.; Danis, P.A. Sun glint correction of the Multi-Spectral Instrument (MSI)-SENTINEL-2 imagery over inland and sea waters from SWIR bands. *Remote Sens. Environ.* **2018**, *204*, 308–321. [[CrossRef](#)]

**Disclaimer/Publisher’s Note:** The statements, opinions and data contained in all publications are solely those of the individual author(s) and contributor(s) and not of MDPI and/or the editor(s). MDPI and/or the editor(s) disclaim responsibility for any injury to people or property resulting from any ideas, methods, instructions or products referred to in the content.